



Remarkable enhancement in visible-light absorption and electron transfer of carbon nitride nanosheets with 1% tungstate dopant

Jing Ding, Li Wang, Qianqian Liu, Yuanyuan Chai, Xin Liu, Wei-Lin Dai*

Department of Chemistry & Shanghai Key Laboratory of Molecular Catalysis and Innovative Materials, Fudan University, Shanghai 200433, PR China

ARTICLE INFO

Article history:

Received 22 January 2015

Received in revised form 11 March 2015

Accepted 19 March 2015

Available online 20 March 2015

Keywords:

Electron transfer

Visible-light absorption

$[\text{WO}_4]^{2-}$ doping $\text{g-C}_3\text{N}_4$

Photocatalysis

Super stability

ABSTRACT

Highly efficient $[\text{WO}_4]^{2-}$ -doped graphitic carbon nitride ($\text{g-C}_3\text{N}_4$) nanosheets were fabricated via a facile and simple method using dicyandiamide and sodium tungstate as precursors. Various analytical techniques were carried out to characterize the $[\text{WO}_4]^{2-}$ -doped $\text{g-C}_3\text{N}_4$ photocatalyst. The results illustrated that $[\text{WO}_4]^{2-}$ intercalated into the interlayers of $\text{g-C}_3\text{N}_4$ nanosheets and bridged with $\text{g-C}_3\text{N}_4$ nanosheets through the unoccupied orbital of tungsten in $[\text{WO}_4]^{2-}$ species and the lone-pair electrons of nitrogen in tris-s-triazine structure, resulting in the enhanced visible light absorption and the electronic structural modulation of $\text{g-C}_3\text{N}_4$. More significantly, the $[\text{WO}_4]^{2-}$ -doped $\text{g-C}_3\text{N}_4$ catalyst exhibited greatly enhanced photocatalytic activity and superior stability for the degradation of organic pollutants (including Rhodamine B, methyl orange and methylene blue) under visible light irradiation. In addition, the underlying photocatalytic reaction mechanism was investigated by the controlled experiments using radical scavengers.

© 2015 Elsevier B.V. All rights reserved.

1. Introduction

Photocatalysis has emerged as one of the most promising and environmental-friendly technologies for organic and inorganic pollutants remediation in wastewater [1,2], clean chemical fuels supplies [3,4] and fine chemicals production [5,6]. However, in order to meet the requirements of practical application, this technology still has two main bottlenecks to be solved: the wide band gap resulting in low solar energy conversion and low quantum efficiency [7]. Hence, seeking a cheap, stable and sustainable photocatalyst with excellent visible-light absorption as well as efficient separation and transportation of the photogenerated holes and electrons is still urgently required.

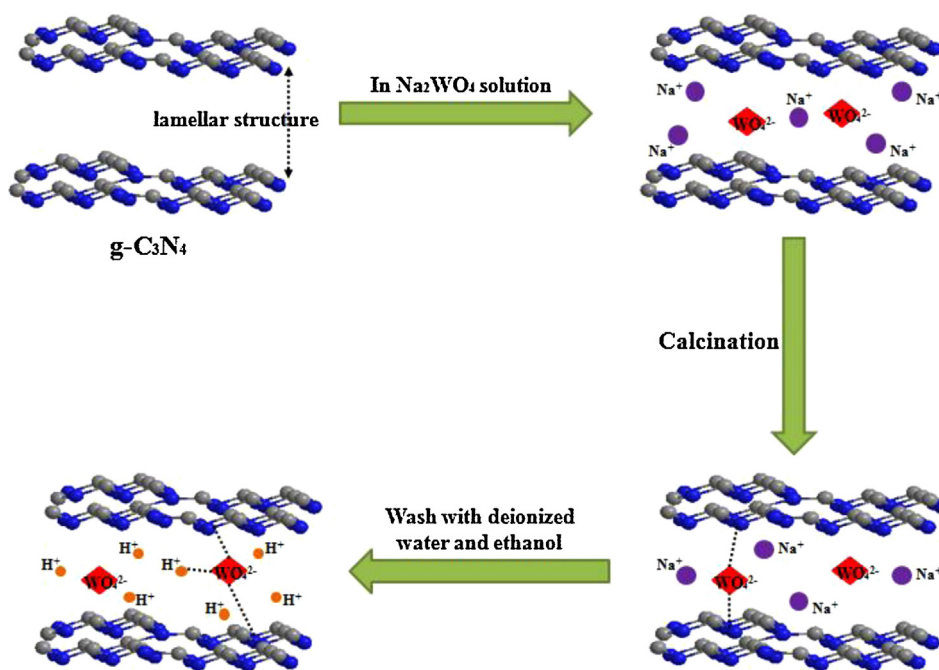
Polymeric graphitic carbon nitride ($\text{g-C}_3\text{N}_4$), an appealing and potential material, has recently received considerable attention in the fields of photocatalysis, gas storage, energy conversion and gas sensors [8,9]. Graphitic carbon nitride, recognized as a promising photocatalyst, possesses a stable heptazine ring structure with a narrow optical band gap of 2.7 eV (the theoretical calculated CB and VB edge potentials are -1.13 and 1.57 eV, respectively) [10]. Moreover, $\text{g-C}_3\text{N}_4$ is easily-synthesized and metal free with a tunable electronic structure. These characters both make $\text{g-C}_3\text{N}_4$ to be

the best candidate for photocatalytic application. Nevertheless, the photocatalytic activity of $\text{g-C}_3\text{N}_4$ is still low due to the poor visible-light response, small BET surface area and slow carrier mobility [11,12]. Hence, many attempts have been made to work out these problems, including metal or non-metal loading, coupling with other semiconductors and chemical doping with foreign elements [13–15].

Modification of semiconductors with the dopants is an effective strategy to finely tune the electronic and optical properties, as well as the conduction band edge of the semiconductors and their surface properties [16–18]. The most prevalent potential dopants for graphitic carbon nitride including iron [19], sulfur [20], phosphorus [21] and potassium [22] have been reported previously. Tungsten is an ideal dopant for minimized crystal defect increase followed by the enhancement of the visible light response and the improvement of the charge separation and transfer [23]. However, up to date, only few studies have reported the use of tungsten doped $\text{g-C}_3\text{N}_4$ as the photocatalyst with obvious improvement on the degradation of organic and inorganic pollutants.

Herein, we firstly report a novel $[\text{WO}_4]^{2-}$ doped $\text{g-C}_3\text{N}_4$ nanosheets photocatalyst with enhanced photocatalytic performance via a simple and facile method using dicyandiamide and sodium tungstate as precursors. The $[\text{WO}_4]^{2-}$ doped $\text{g-C}_3\text{N}_4$ nanosheets enhanced visible-light absorption and electron transfer properties. Simultaneously, the catalyst was successfully applied in the photocatalytic degradation of the organic pollutants under

* Corresponding author. Tel: +86 5566 4678; fax: +86 5566 5572.
E-mail address: wldai@fudan.edu.cn (W.-L. Dai).



Scheme 1. Schematic representation of the synthesis process of $[\text{WO}_4]^{2-}$ -(Xwt.%) -CN catalyst.

visible light irradiation, exhibiting highly photocatalytic activity in comparison to pure $\text{g-C}_3\text{N}_4$. Moreover, stability of the synthesized photocatalyst was investigated and the possible photocatalytic mechanism was proposed in detail.

2. Experimental

2.1. Preparation of $[\text{WO}_4]^{2-}$ -doped $\text{g-C}_3\text{N}_4$ nanosheets ($[\text{WO}_4]^{2-}$ -CN)

All the reagents were purchased from Sinopharm Chemical Reagent Co., Ltd., without further purification, unless otherwise specified. The $\text{g-C}_3\text{N}_4$ nanosheets with different contents of $[\text{WO}_4]^{2-}$ were synthesized by a conventional incipient wetness impregnation method. The schematic illustration of the synthesis of $[\text{WO}_4]^{2-}$ -(Xwt.%) -CN could be identified during the process, as described in Scheme 1. In a typical process, 5 g of dicyandiamide powder was dispersed in 30 mL deionized water and heated at 65°C for 0.5 h under stirring. Then, a certain amount of Na_2WO_4 was added to the above solution, and the temperature was risen to 100°C for complete water evaporation, followed by milling and annealing at 550°C under air atmosphere for 3 h with ramping rate of $2^\circ\text{C}/\text{min}$. The resultant powders were washed for several times with deionized water and ethanol to remove any soluble impurities (including Na^+), and dried overnight at 70°C in vacuum oven. The as-prepared catalysts were denoted as $[\text{WO}_4]^{2-}$ -(Xwt.%) -CN in which X stood for the weight content (Xwt.%) of Na_2WO_4 to dicyandiamide. In the present work, $[\text{WO}_4]^{2-}$ -(0.5 wt.%) -CN, $[\text{WO}_4]^{2-}$ -(1 wt.%) -CN, $[\text{WO}_4]^{2-}$ -(4 wt.%) -CN and $[\text{WO}_4]^{2-}$ -(10 wt.%) -CN were, respectively, prepared to investigate the degradation of Rhodamine B. Meanwhile, pure $\text{g-C}_3\text{N}_4$ nanosheets (CN) were prepared under identical conditions as the synthesis of $[\text{WO}_4]^{2-}$ -(Xwt.%) -CN but without Na_2WO_4 addition.

2.2. Characterizations

X-ray diffraction (XRD) patterns were recorded on a Bruker D8 advance spectrometer with $\text{Cu K}\alpha$ radiation ($\lambda = 0.154\text{ nm}$),

operated at 40 mA and 40 kV. UV-vis spectroscopy measurement was carried out on a Shimadzu UV-3600 UV-vis-NIR spectrophotometer with BaSO_4 as a reflectance standard. The FT-IR spectra were carried out on a Nicolet Avatar-360 FT-IR spectrometer. The Laser Raman experiments were performed with a Jobin Yvon Dilor Labram I Raman spectrometer equipped with a holographic notch filter, CCD detector, and He-Ne laser radiating at 632.8 nm. Nitrogen adsorption-desorption isotherms were measured on a Micromeritics Tristar 3000 system. Samples were degassed at 250°C on a vacuum line for 3 h. Specific surface areas were calculated by utilizing a standard Brunauer-Emmett-Teller (BET) method. Transmission electron microscope (TEM) images were obtained on a JOEL JEM 2010 transmission electron microscope. The samples were supported on carbon-coated copper grids for the experiment. The X-ray photoelectron spectra (XPS) were obtained on a RBD 147 upgraded PHI 5000C ESCA system equipped with a dual X-ray source, of which the $\text{Mg K}\alpha$ (1253.6 eV) anode and a hemispherical energy analyzer were used. The background pressure during data acquisition was maintained at $<10^{-6}$ Pa. Measurements were performed at a pass energy of 93.90 eV. All binding energies were calibrated using contaminant carbon ($\text{C1s} = 284.6\text{ eV}$). Photoluminescence spectra (PL) of the samples were obtained using a fluorescence spectrometer (Hitachi F-4500) using a Xe lamp as excitation source.

2.3. Photodegradation reaction

The photocatalytic performances of the as-prepared $[\text{WO}_4]^{2-}$ -(Xwt.%) -CN were evaluated by the degradation of Rhodamine B (RhB) under visible light irradiation ($\lambda > 420\text{ nm}$). Visible irradiation was obtained from a 300 W Xe lamp with a 420 nm cutoff filter. In each experiment, 100 mg of photocatalyst was dispersed in 100 mL aqueous solution of RhB (10 ppm) in an ultrasound generator for 5 min. Prior to irradiation, the suspension was magnetically stirred in the darkness for 30 min to obtain the absorption-desorption equilibrium. During the photodegradation reaction, 3 mL of RhB solution with catalyst was sampled at the certain time intervals and centrifuged to remove the solid

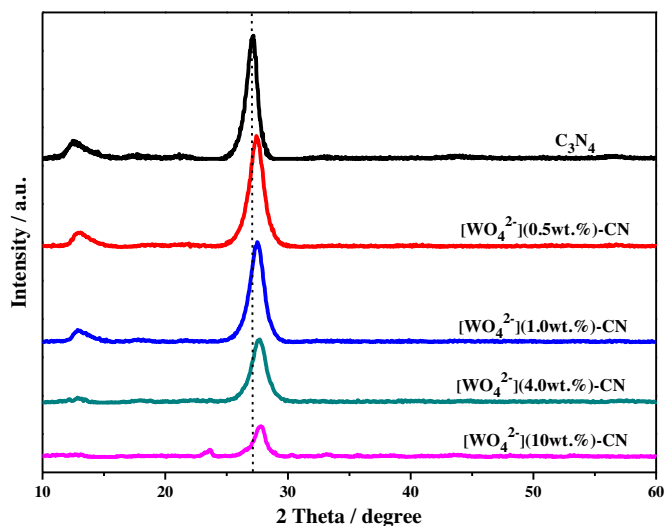


Fig. 1. XRD patterns of g-C₃N₄ and [WO₄]²⁻(Xwt.%)CN samples as-prepared at 550 °C calcination temperature.

photocatalyst. The concentration of RhB was determined by means of a UV–vis spectrophotometer at a wavelength of 550 nm.

3. Results and discussion

3.1. Characterizations of [WO₄]²⁻(Xwt.%)CN

The changes of the phase structure before and after doping [WO₄]²⁻ were investigated by XRD. As shown in Fig. 1, the two pronounced diffraction peaks at $2\theta = 27.3^\circ$ and 13.3° match well with the (002) and (100) diffraction planes of layered g-C₃N₄. The strong diffraction peak at 27.3° , indexed as the (002) peak, is a characteristic interlayer stacking reflection of conjugated aromatic systems. The weak one at 13.3° is related to in-planar tris-s-triazine structural packing motif with the distance around 0.665 nm [24]. In comparison with pure g-C₃N₄, the (100) diffraction peak intensities of W(Xwt.%)CN obviously decrease with the increasing of [WO₄]²⁻ content, indicating that the host-guest interactions between [WO₄]²⁻ species and the big C–N rings of g-C₃N₄ through the unoccupied orbital of tungsten in [WO₄]²⁻ species and the lone-pair electrons of nitrogen in tris-s-triazine structure, thus, altering the electronic structure and in-plane tris-s-triazine repeating network [25]. Besides, the (002) diffraction peak position for [WO₄]²⁻(Xwt.%)CN gradually shifts to the higher angle than that of the pure g-C₃N₄ and the (002) diffraction peak intensity of

[WO₄]²⁻(Xwt.%)CN distinctly grows weaker with the increasing of [WO₄]²⁻ doping content, implying that [WO₄]²⁻ ions intercalate into and interact with the interlayers of g-C₃N₄ nanosheets through N-bridge linking of the triazine units. However, when the amount of [WO₄]²⁻ content reaches up to 10 wt.%, some diffraction peaks for relevant W species appear. It is presumably owing to that excess doping results in the crystals aggregation and crystallization on the surface of g-C₃N₄ nanosheets.

Optical absorption of pure g-C₃N₄ and [WO₄]²⁻(Xwt.%)CN system studied by UV–vis diffuse reflectance spectroscopy was displayed in Fig. 2. As demonstrated in Fig. 2a, pure g-C₃N₄ shows a typical semiconductor absorption, whose adsorption edges are located approximately at 460 nm. Notably, with the increasing [WO₄]²⁻ ions in [WO₄]²⁻(Xwt.%)CN system, the absorption edges gradually red-shifts, even extending to more than 650 nm, which demonstrates the existence of the strong interaction between [WO₄]²⁻ and nitrogen pots of the lattice of g-C₃N₄ and the change of its own electronic structure. Undoubtedly, these observations suggest that more visible light can be harvested and photoinduced electrons and holes can be produced more easily, further inoculated with the enhanced photocatalytic activity [26]. In addition, the band gap energy calculated based on the Oregan and Gratzel method indicates that the value for g-C₃N₄ is 2.70 eV, accorded well with previous literatures [10]. For [WO₄]²⁻(Xwt.%)CN system, it can be clearly observed in Fig. 2b that the optical band gap energies of [WO₄]²⁻(0.5 wt.%)CN, [WO₄]²⁻(1.0 wt.%)CN, [WO₄]²⁻(4.0 wt.%)CN and [WO₄]²⁻(10 wt.%)CN are 2.68, 2.64, 2.61 and 2.52 eV, respectively. Obviously, the band gap energies slightly decrease accompanied with the increasing content of [WO₄]²⁻ ions, implying that [WO₄]²⁻ doping content strongly affects the optical property of [WO₄]²⁻(Xwt.%)CN system and the ability of visible light response.

To characterize the specific surface area of g-C₃N₄ and [WO₄]²⁻(Xwt.%)CN, the nitrogen adsorption and desorption isotherms were measured and listed in Table 1. The BET surface area (S_{BET}) of [WO₄]²⁻(Xwt.%)CN initially increases from 13 to 46 m² g⁻¹, then gradually decrease to 30 m² g⁻¹. Interestingly, the BET surface area obviously increases after doping [WO₄]²⁻ ions, even the S_{BET} of [WO₄]²⁻(1.0 wt.%)CN increases by nearly 4 times as that of the pristine g-C₃N₄ (13–46 m² g⁻¹), suggesting that g-C₃N₄ sheets are unfolded by slightly doping [WO₄]²⁻ ions to increase the BET surface area. The larger S_{BET} will contribute to facilitating adsorption, desorption and diffusion of reactants and products and providing more possible reaction sites [27], which are conducive to the enhanced photocatalytic activity. Moreover, with the increased amount of [WO₄]²⁻ ions, the pore volume and average pore diameter in Table 1 also exhibit the same variation trend

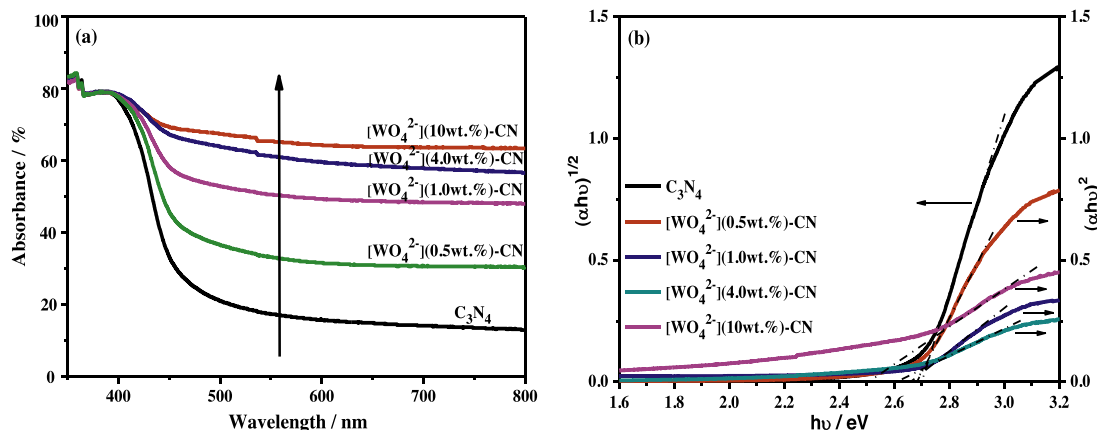


Fig. 2. (a) UV–vis absorption spectra of g-C₃N₄ and [WO₄]²⁻(Xwt.%)CN samples and (b) diffuse reflectance spectra of g-C₃N₄ and [WO₄]²⁻(Xwt.%)CN samples.

Table 1
Physicochemical characterization of $[\text{WO}_4]^{2-}$ -(Xwt.%)–CN samples.

Entry	Samples	S_{BET} ($\text{m}^2 \text{g}^{-1}$)	Pore volume (cc g^{-1})	Average pore diameter (nm)
1	g- C_3N_4	13	0.0087	2.6
2	$[\text{WO}_4]^{2-}$ -(0.5wt.%)–CN	24	0.0144	2.8
3	$[\text{WO}_4]^{2-}$ -(1.0wt.%)–CN	46	0.0283	2.9
4	$[\text{WO}_4]^{2-}$ -(4.0wt.%)–CN	42	0.0260	2.6
5	$[\text{WO}_4]^{2-}$ -(10wt.%)–CN	30	0.0188	2.4

as the S_{BET} results, further implying that these pores originate from the stacking of g- C_3N_4 sheets and $[\text{WO}_4]^{2-}$ ions strongly interact with the interlayers of g- C_3N_4 nanosheets through N-bridge linking to increase the space between interlayers in the wake of $[\text{WO}_4]^{2-}$ ions doping.

A comparison of $[\text{WO}_4]^{2-}$ -(Xwt.%)–CN to pure g- C_3N_4 in functional groups of chemical structure was monitored by FT-IR spectroscopy as shown in Fig. S1. The broad peaks at approximately 3150 and 3450 cm^{-1} can be attributed to the stretching vibrational modes of residual N–H components and O–H bonds, associated with uncondensed amino groups and absorbed H_2O molecule [28,29]. Interestingly, with the increasing of $[\text{WO}_4]^{2-}$ content in $[\text{WO}_4]^{2-}$ -(Xwt.%)–CN, the band at 3150 cm^{-1} corresponding to the –NH on the surface of g- C_3N_4 grows stronger, indicating that $[\text{WO}_4]^{2-}$ is coordinated with nitrogen pots of pre-polymer (dicyandiamide) and results in the more incomplete polymerization of amino groups. In addition, a new vibrational peak at around 2200 cm^{-1} attributed to the stretching vibrations of the defects of $\text{C}\equiv\text{N}$ groups [22], can be found and enhanced with the increasing of the doping $[\text{WO}_4]^{2-}$ amount, further suggesting that the strong chemical coordination between $[\text{WO}_4]^{2-}$ and N atoms in the “nitrogen pots” of pre-polymer and the unique chemical structure acquired. More importantly, the improved chemical structure, in principle, is beneficial for charge separation and migration within the polymeric matrix, due to the presence of less structural imperfection (promoting electron delocalization) in conjugated network [30]. Meanwhile, $[\text{WO}_4]^{2-}$ -(Xwt.%)–CN exhibits a new peak centered at around 3300 cm^{-1} followed by the increasing of $[\text{WO}_4]^{2-}$ content, which could be assigned to the –OH stretching mode of tungstic acid [31]. That is, $[\text{WO}_4]^{2-}$ eventually in the form of tungstic acid exists in the interlayers of g- C_3N_4 sheets, as confirmed by XPS results. What is more, several bands in the region ranging from 1200 to 1650 cm^{-1} (1245, 1326, 1410, 1560 and 1650 cm^{-1}) are assigned to C–NH–C and C=N stretching vibration modes of heterocycles [32,33] and the sharp characteristic peak located at around 808 cm^{-1} is indexed to the triazine ring stretching vibration as well, whose peaks come to slightly red-shift in comparison with pure g- C_3N_4

[34]. This phenomenon ulteriorly indicates that $[\text{WO}_4]^{2-}$ intercalates into the interlayers of g- C_3N_4 nanosheets and interacts with triazine units and aromatic systems of g- C_3N_4 nanosheets strongly.

The Raman spectra, as shown in Fig. S2, illustrated additional information for the structure of $[\text{WO}_4]^{2-}$ -(Xwt.%)–CN system. The bands at approximately 707, 790, 980 and 1210 cm^{-1} are corresponded to the different types of ring breathing modes of s-triazine in the C_3N_4 crystal structure [35]. Compared with pure g- C_3N_4 , all the characteristic bands mentioned above appear in the $[\text{WO}_4]^{2-}$ -(1.0wt.%)–CN sample and no additional peaks come out, which demonstrates that the geometry structure of C_3N_4 still keeps unchanged after doping $[\text{WO}_4]^{2-}$. Notably, the corresponding peaks of $[\text{WO}_4]^{2-}$ -(1.0wt.%)–CN sample grow weakened and slightly blue-shift. This phenomenon may be attributed to a guest-host synergistic effect between $[\text{WO}_4]^{2-}$ and in-plane/interlayer structure of g- C_3N_4 nanosheets, which is in accord with the results of FT-IR and XRD.

The morphology and microstructure of the as-obtained g- C_3N_4 and $[\text{WO}_4]^{2-}$ -(1.0wt.%)–CN sample were visualized via TEM. As demonstrated in Fig. S3a, pure g- C_3N_4 displays a graphite-like lamellar structure with wrinkles and rolling edges structure. In contrast, Fig. 3a shows that the $[\text{WO}_4]^{2-}$ -(1.0wt.%)–CN sample exhibits irregular porous structure besides the typical layered stacked structure, which is mainly attributed to the synergistic effect between $[\text{WO}_4]^{2-}$ and N atoms in the “nitrogen pots” of pre-polymer/interlayer structure of C_3N_4 nanosheets to create the bigger pores. This result is well consistent with the BET data. Notably, the hierarchical porous structures can contribute to promote the separation of the electron–hole pairs and offer more active sites [36]. From Fig. 3b, the high-resolution TEM (HR-TEM) image illustrates the interlayer distance of the (002) diffraction plane of $[\text{WO}_4]^{2-}$ -(1.0wt.%)–CN is around 0.355 nm, larger than that of pure g- C_3N_4 (0.324 nm) reported previously [37]. This observation indicates that $[\text{WO}_4]^{2-}$ inserted successfully into the hierarchical structure of C_3N_4 nanosheets, thus, increasing the space of the crystal facet (002) of g- C_3N_4 , identical to the results of BET. In

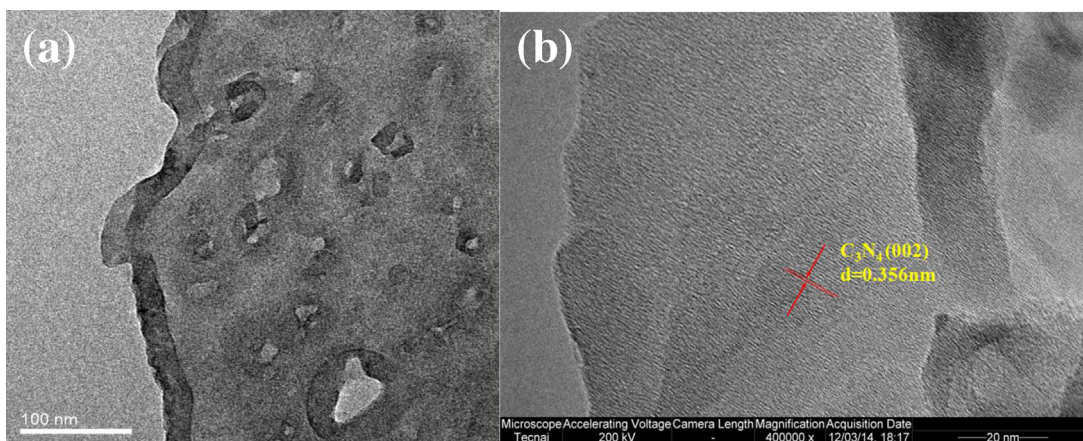


Fig. 3. (a) TEM images of $[\text{WO}_4]^{2-}$ -(1.0wt.%)–CN sheets and (b) HR-TEM of images of $[\text{WO}_4]^{2-}$ -(1.0wt.%)–CN sample.

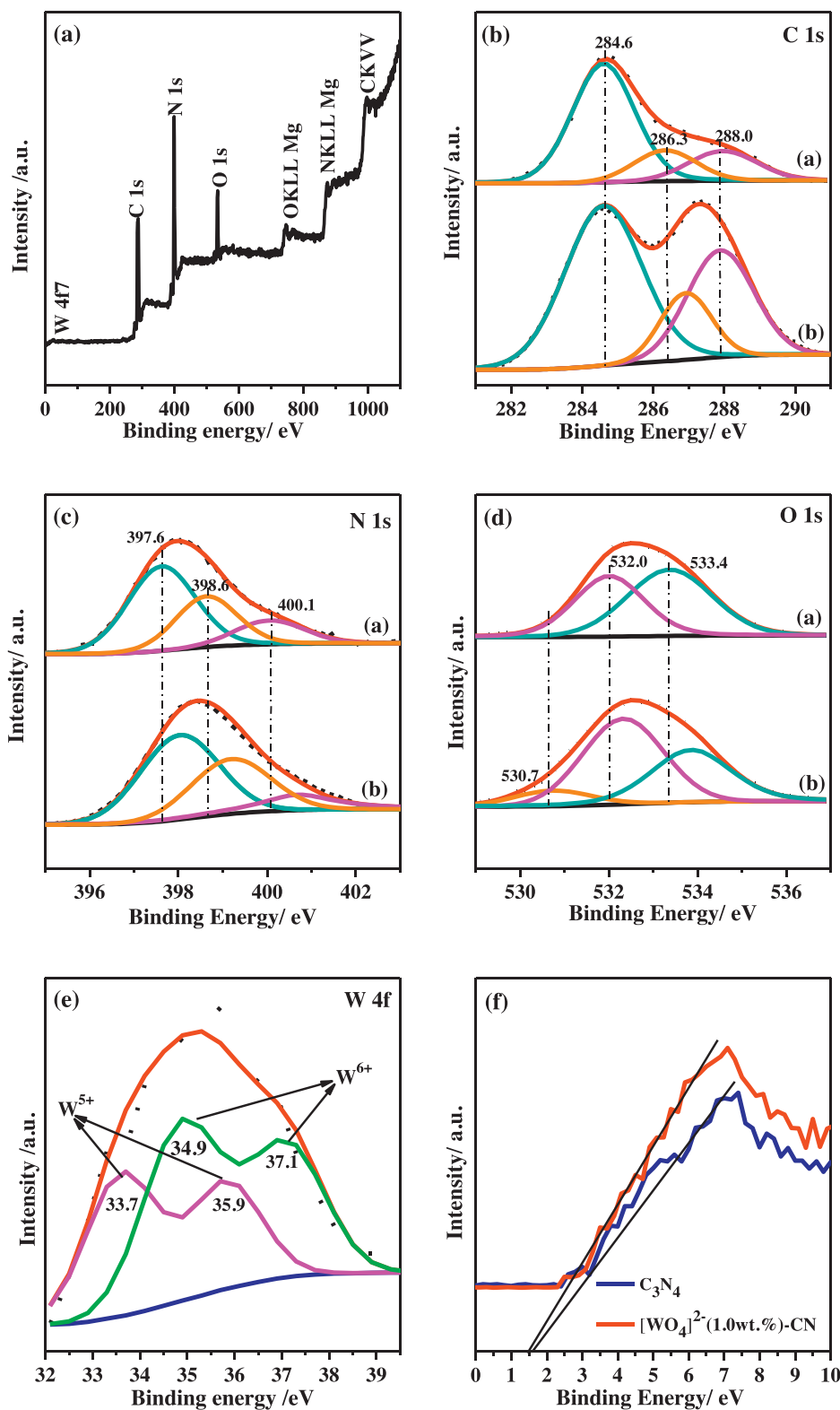


Fig. 4. XPS spectra of g-C₃N₄ (a) and [WO₄]²⁻(1.0 wt.%)CN (b): (a) the survey spectrum of [WO₄]²⁻(1.0 wt.%)CN; (b) high-resolution C1s; (c) high-resolution N1s; (d) high-resolution O1s; (e) high-resolution W4f of [WO₄]²⁻(1.0 wt.%)CN; (f) the valence band spectrum.

addition, energy dispersive X-ray spectroscopy (EDX) shown in Fig. S3b, resulting from selected area, revealed that C, N, O and W elements existed in the [WO₄]²⁻(1.0 wt.%)CN, which demonstrates that Na⁺ is fully substituted for H⁺ and [WO₄]²⁻ ultimately in “tungstic acid” form exists in the interlayers of g-C₃N₄ sheets. This speculation can be further attested by XPS in Fig. 4 and Fig. S6.

To characterize in-depth, the chemical composition and electronic structure of g-C₃N₄ and [WO₄]²⁻(1.0 wt.%)CN, XPS were carried out. As observed in Fig. 4a, the [WO₄]²⁻(1.0 wt.%)CN sample contains C, N, O and W with obvious photoelectron peaks at binding energies of 35 (W4f), 288 (C1s), 400 (N1s) and 533 eV (O1s). Compared with the spectra of pure g-C₃N₄ in Fig. 4b and

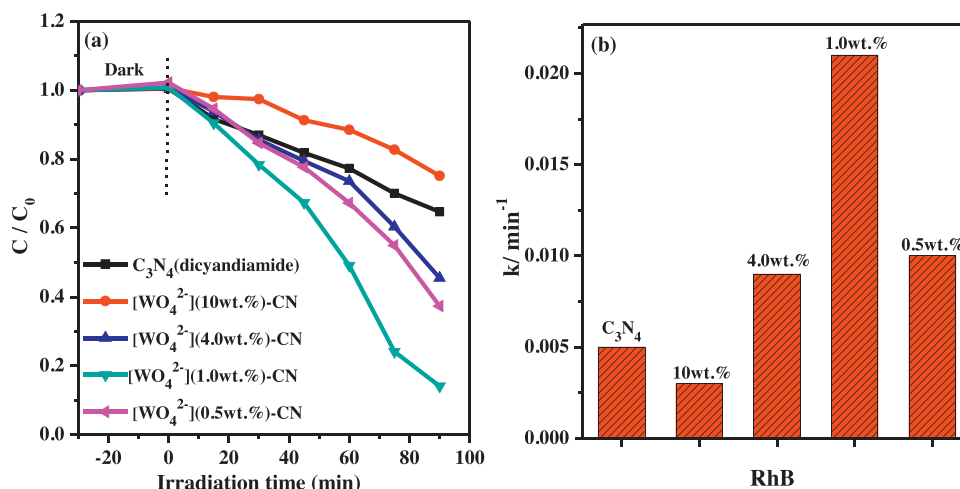


Fig. 5. (a) The photocatalytic performance of g- C_3N_4 and $[WO_4]^{2-}$ (Xwt.%)CN catalysts and (b) apparent rate constants of g- C_3N_4 and $[WO_4]^{2-}$ (Xwt.%)CN catalysts for the degradation of RhB under visible light.

c, the C1s and N1s peaks of the $[WO_4]^{2-}$ (1.0 wt.%)CN sample show nearly identical pattern, implying that the lamellar structure of graphite C_3N_4 is still preserved after doping with $[WO_4]^{2-}$. In Fig. 4b, the C1s spectrum of both g- C_3N_4 and $[WO_4]^{2-}$ (1.0 wt.%)CN can be deconvoluted into three peaks centered at 284.6, 286.3 and 288.0 eV. The three peaks are, respectively, ascribed to the sp^2 C–C bonds of graphitic carbon, the sp^2 -bond carbon (N–C=N) in the s-triazine rings and the sp^2 -hybridized C atoms in the aromatic ring attached to terminal uncondensed amino groups (e.g., $-NH_2$ and $-NH$) [38–40]. However, in comparison with pure g- C_3N_4 , the obvious shifts to higher binding energies can be observed for $[WO_4]^{2-}$ (1.0 wt.%)CN, which reveals the strong interaction between $[WO_4]^{2-}$ and the in-plane carbon (N–C=N) in the s-triazine rings as well as the nitrogen (C–NH₂) on the surface of graphitic C_3N_4 , further demonstrating that $[WO_4]^{2-}$ ions are inserted into the layers of g- C_3N_4 nanosheets and change the electron density of g- C_3N_4 . The N1s spectra in Fig. 4c clearly display the presence of three distinct N species. The peaks located at 397.6, 398.6 and 400.1 eV are originated from the sp^2 hybridized aromatic N atoms bonded to carbon atoms (C–N=C), the tertiary nitrogen (N–C₃) and the uncondensed amino groups (–NH) [41–43]. Similarly, the obvious shifts to higher binding energies are observed in

N1s region of $[WO_4]^{2-}$ (1.0 wt.%)CN compared to that of g- C_3N_4 , illustrating that more W–N bonds are formed and cause the lower electron density of N atoms. As shown in Fig. 4d, the O1s peaks at 533.4 and 532.0 eV can originate from adsorbed water and O₂ [44,45]. Besides these two O1s peaks, a new peak at low binding energy of 530.7 eV appeared in the $[WO_4]^{2-}$ (1.0 wt.%)CN. This is probably attributed to the W–O–H groups, as reported previously [46]. What is more, from Fig. 4e, the W4f spectra can be divided into two peaks at 35.9 eV and 34.9 eV for the W4f spin-orbit components, which can be attributed to the presence of tungsten in the form of W(V) (BE W4f7/2 = 34.9 eV) and W(VI) (BE W4f7/2 = 35.9 eV) species [47]. In addition, the valence band (VB) XPS was applied to determine the electronic structure. Fig. 4f shows $[WO_4]^{2-}$ (1.0 wt.%)CN locates at the lower VB (1.54 eV) than that of pure g- C_3N_4 (1.57 eV). Both two VB of $[WO_4]^{2-}$ (1.0 wt.%)CN and g- C_3N_4 are completely consistent with that of calculations by the Mulliken electronegativity theory [48]. These results suggest that the electronic structure of g- C_3N_4 is changed by doping $[WO_4]^{2-}$ and more photoinduced electrons and holes can be easily produced, thus, improving the photocatalytic degradation ability.

3.2. Photocatalytic performance and photoluminescence

The photocatalytic capability of pristine g- C_3N_4 , as well as $[WO_4]^{2-}$ (Xwt.%)CN catalyst, was evaluated for the degradation of RhB under visible light. As shown in Fig. 5a, dark adsorption of RhB dye was measured for 30 min to check the self-graftation. Apparently, there is no adsorption phenomenon in pure g- C_3N_4 and $[WO_4]^{2-}$ (Xwt.%)CN systems. The $[WO_4]^{2-}$ (Xwt.%)CN photocatalyst exhibits much higher photocatalytic activity than pure g- C_3N_4 . Meanwhile, $[WO_4]^{2-}$ (1.0 wt.%)CN photocatalyst ($k = 0.022 \text{ min}^{-1}$) displays the highest rate constant, which is 4.4 times as high as that of g- C_3N_4 ($k = 0.005 \text{ min}^{-1}$). The enhancement can be attributed to the synergistic effect of decreased band gap energy, the reduction of recombination rate of photogenerated electron–hole pairs and the increase of adsorption, desorption and diffusion of reactants and products. Obviously, $[WO_4]^{2-}$ (1.0 wt.%)CN displays the highest activity of all the $[WO_4]^{2-}$ (Xwt.%)CN system. When the $[WO_4]^{2-}$ amount exceeds 1.0 wt.%, the photodegradation activity of $[WO_4]^{2-}$ (Xwt.%)CN catalyst gradually decreased. The phenomena can be ascribed to the excess $[WO_4]^{2-}$ doped and will hinder the adsorption of visible light and reactants on the surface of g- C_3N_4 , and thus, reduce the efficiency of charge transfer. Furthermore, the $[WO_4]^{2-}$ (1.0 wt.%)CN photocatalyst was applied to the

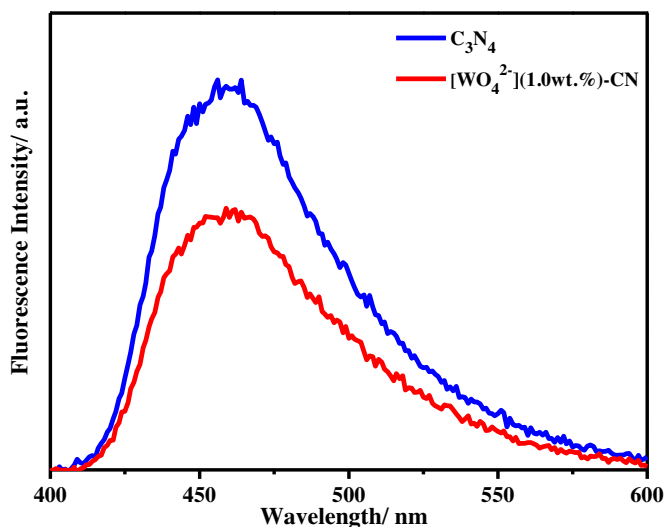


Fig. 6. Photoluminescence emission spectra of g- C_3N_4 and $[WO_4]^{2-}$ (1.0 wt.%)CN catalyst.

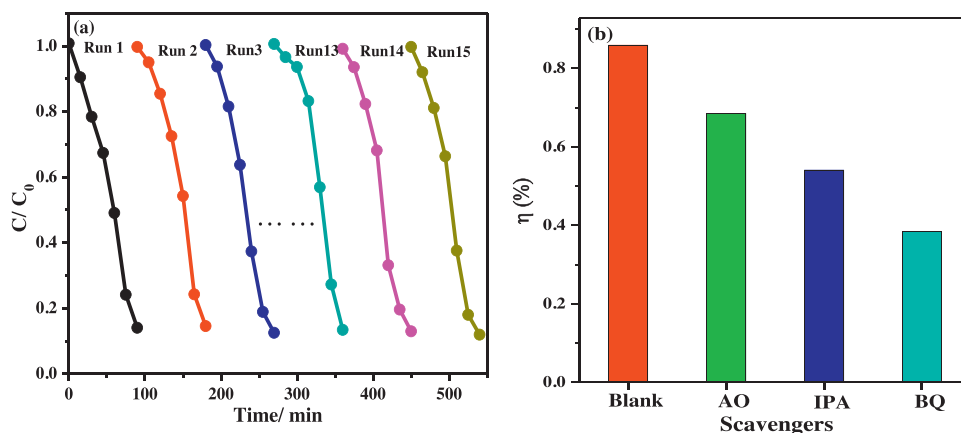


Fig. 7. (a) The reusability of the [WO₄]²⁻ (1.0 wt.%)–CN photocatalyst for the photocatalytic degradation of RhB and (b) effects of various scavengers on the visible light photocatalytic activity of [WO₄]²⁻ (1.0 wt.%)–CN.

photodegradation of other organic pollutants. From Fig. S4a and b, the [WO₄]²⁻ (1.0 wt.%)–CN exhibits enhanced photocatalytic activity of photodegradation of methyl orange (MO) and methylene blue (MB), which is approximately 2.2 and 1.4 times as that of pure g-C₃N₄. In addition, the corresponding first-order kinetic plot (see Fig. S4c) further implies that [WO₄]²⁻ (1.0 wt.%)–CN shows the higher degradation rate.

The efficient photogenerated electron–hole pair separation ability of g-C₃N₄ based photocatalyst was investigated by photoluminescence (PL) spectra. Fig. 6 exhibits the PL spectra of pristine g-C₃N₄ and [WO₄]²⁻ (1.0 wt.%)–CN under the excitation wavelength of 365 nm. Obviously, apparent emission peaks of g-C₃N₄ and [WO₄]²⁻ (1.0 wt.%)–CN appear at approximately 455 nm, which is ascribed to the direct electrons and holes recombination of band transition. Compared to pristine g-C₃N₄, the PL intensity of [WO₄]²⁻ (1.0 wt.%)–CN drops substantially, suggesting that [WO₄]²⁻ (1.0 wt.%)–CN displays more photogenerated electrons and holes produced and lower recombination probability of photogenerated charge carriers, thus, improving the photocatalytic activity.

3.3. Stability evaluation

The long-term recyclability and stability of a photocatalyst were crucial for practical application. To assess the reusability of the [WO₄]²⁻ (1.0 wt.%)–CN photocatalyst, successive photocatalytic experiments were carried out by adding the same amount of the recycled [WO₄]²⁻ (1.0 wt.%)–CN photocatalyst to fresh RhB solutions (10 mg/L) under visible-light irradiation. The photocatalytic performance of [WO₄]²⁻ (1.0 wt.%)–CN for the degradation of RhB keeps constant in fifteen successive experimental runs under the same experimental conditions (see Fig. 7). Moreover, Compared the XRD pattern of the fresh catalyst to that of the reused one (Fig. S5a), no obvious change can be observed, which hints that the high structural stability of [WO₄]²⁻ (1.0 wt.%)–CN photocatalyst and [WO₄]²⁻ is strongly bonded with the interlayers of g-C₃N₄ sheets through the unoccupied orbital of tungsten in [WO₄]²⁻ species and the lone-pair electrons of nitrogen in tris-s-triazine structure. Surprisingly, the other method, employed to evaluate the reusability of the [WO₄]²⁻ (1.0 wt.%)–CN photocatalyst, makes a big difference with the one mentioned above. As shown in Fig. S5b, the photocatalytic activity of [WO₄]²⁻ (1.0 wt.%)–CN photocatalyst for the degradation of RhB significantly enhances in six successive experimental runs and keep unchanged after five experimental runs. This phenomenon goes somewhat against the results of relevant literatures reported previously [49]. One feasible explanation for the enhancement after successive experimental runs in

the [WO₄]²⁻ (1.0 wt.%)–CN is given as follows. The superoxide radicals can be stabilized by tungsten species and tungsten species suppress rapid combination of the superoxide radical ($\cdot\text{O}_2^-$) with hydrogen ions (H^+) to form water (H_2O) [50,51]. Moreover, due to the superoxide radical ($\cdot\text{O}_2^-$) as the main active species in the current photocatalytic reaction and more superoxide radical generated after many times' recycling without taking out the catalyst, the apparent reaction rate obviously grows higher.

3.4. Possible photocatalytic mechanism

To check the reaction mechanism in depth, the active species generated during the reaction process are identified by hole and free radical trapping experiment. Ammonium oxalate (AO), isopropanol (IPA) and 1,4-benzoquinone (BQ) were used as the hole (h^+) scavenger, hydroxyl radical ($\cdot\text{OH}$) scavenger and superoxide radical ($\cdot\text{O}_2^-$) scavenger, respectively [52]. As shown in Fig. 7, the photocatalytic activity of [WO₄]²⁻ (1.0 wt.%)–CN decreases slightly by the addition of hole scavengers but reduces greatly with the addition of superoxide radical scavengers and hydroxyl radical scavengers, indicating that $\cdot\text{O}_2^-$ and $\cdot\text{OH}$ are the main oxidative species for [WO₄]²⁻ (1.0 wt.%)–CN in these photocatalytic systems. Accordingly, a possible photocatalytic oxidation mechanism for the RhB degradation by [WO₄]²⁻ (1.0 wt.%)–CN photocatalyst was briefly described in Fig. 8. Under the visible light irradiation, the [WO₄]²⁻ (1.0 wt.%)–CN catalyst can be excited and then produces

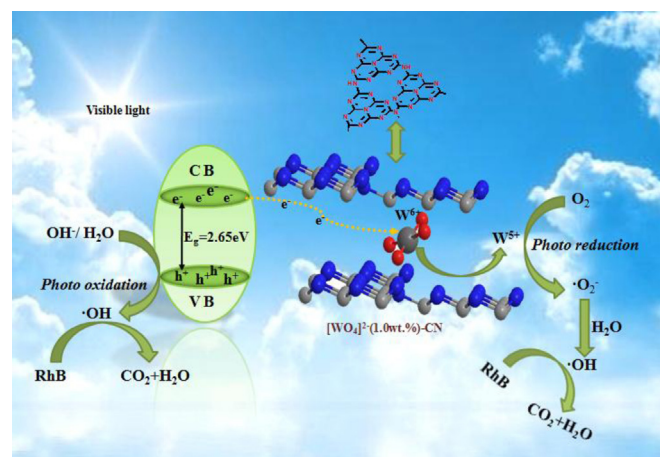


Fig. 8. Possible degradation mechanism of RhB over [WO₄]²⁻ (1.0 wt.%)–CN photocatalyst under visible light irradiation.

photogenerated electrons and holes. The photogenerated electrons trapped by the W^{6+} species can react with electron acceptors such as the surface adsorptive O_2 , to form superoxide anion $\bullet O_2^-$ [53]. The W^{6+} species can act as a trap center for the photo-induced electrons, resulting in the reduction of the electrons and holes recombination. Meanwhile, valance holes oxidize OH^- or H_2O molecules to $\bullet OH$. In addition, the C_3N_4 sheets bridged by $[WO_4]^{2-}$ ions can act as a superior transporter and modulate the electronic structure of g- C_3N_4 to prolong the lifetime of charge carriers, improving the separation efficiency of the holes and electrons.

4. Conclusion

In summary, we firstly demonstrate here a simple and large-scale method to prepare highly efficient $[WO_4]^{2-}$ doped g- C_3N_4 nanosheets. $[WO_4]^{2-}$ doping enhanced visible light absorption by narrowing the band gap to get more visible light harvested and produce photo-induced electrons and holes more easily. Meanwhile, C_3N_4 nanosheets bridged by $[WO_4]^{2-}$ ions can act as a superior electron transporter and modulate the electronic structure of g- C_3N_4 to prolong the lifetime of charge carriers. Moreover, the $[WO_4]^{2-}$ doped g- C_3N_4 catalyst exhibits enhanced photocatalytic performance and high stability after fifteen successive experimental runs without any obvious change in the activity. The present study puts forward the possibility of utilizing $[WO_4]^{2-}$ anion as a general dopant to enhance visible-light absorption and electron transport properties for other semiconductors, which might open novel vistas for exploring anion doping in various optoelectronic applications.

Acknowledgments

We would like to thank financial support by the Major State Basic Research Development Program (Grant No. 2012CB224804), NSFC (Project 21373054, 21173052), State Key Laboratory of Catalytic Materials and Reaction Engineering (RIPP, SINOPEC) and the Natural Science Foundation of Shanghai Science and Technology Committee (08DZ2270500).

Appendix A. Supplementary data

Supplementary data associated with this article can be found, in the online version, at <http://dx.doi.org/10.1016/j.apcatb.2015.03.028>.

References

- [1] T.L. Thompson, J.T. Yates, Chem. Rev. 106 (2006) 4428.
- [2] M.R. Hoffmann, S.T. Martin, W. Choi, D.W. Bahnemann, Chem. Rev. 95 (1995) 69.
- [3] M. Conte, A. Iacobazzi, M. Ronchetti, R. Vellone, J. Power Source 100 (2001) 171.
- [4] L. Barreto, A. Makihiro, K. Riahi, J. Hydrogen Energy 28 (2003) 267.
- [5] Y. Shiraishi, S. Kanazawa, Y. Sugano, D. Tsukamoto, H. Sakamoto, S. Ichikawa, ACS Catal. 4 (2014) 774.
- [6] X. Dai, M.L. Xie, S.G. Meng, X.L. Fu, S.F. Chen, Appl. Catal. B: Environ. 158–159 (2014) 382.
- [7] L.M. Sun, X. Zhao, C.J. Jia, Y.X. Zhou, X.F. Cheng, P. Li, J. Mater. Chem. 22 (2012) 23428.
- [8] Y. Wang, X.C. Wang, M. Antonietti, Angew. Chem. Int. Ed. 51 (2012) 68.
- [9] X. Wang, K. Maeda, A. Thomas, K. Takanabe, G. Xin, J.M. Carlsson, Nat. Chem. 8 (2009) 76.
- [10] A. Thomas, A. Fischer, F. Goettmann, M. Antonietti, J.O. Muller, R. Schlögl, J. Mater. Chem. 18 (2008) 4893.
- [11] S.B. Yang, Y.J. Gong, J.S. Zhang, L. Zhan, L.L. Ma, Z.Y. Fang, Adv. Mater. 25 (2013) 2452.
- [12] Y.J. Zhang, A. Thomas, M. Antonietti, X.C. Wang, J. Am. Chem. Soc. 131 (2008) 50.
- [13] M. Gopa, C.B. Gobinda, S.K. Singh, K.M. Parida, Dalton Trans. 41 (2012) 14299.
- [14] D.M. Chen, K.W. Wang, D.G. Xiang, R.L. Zong, W.Q. Yao, Y.F. Zhu, Appl. Catal. B: Environ. 147 (2014) 554.
- [15] Y. Wang, J.S. Zhang, X.C. Wang, M. Antonietti, H.R. Li, Angew. Chem. Int. Ed. 49 (2010) 3356.
- [16] X. Li, J. Zhu, H.X. Li, Catal. Commun. 24 (2012) 20.
- [17] J.P. Huang, J. Xu, H.X. Li, H.S. Luo, X.B. Yu, Y.K. Li, J. Solid State Chem. 184 (2011) 843.
- [18] J.G. Wang, P. Zhang, X. Li, J. Zhu, H.X. Li, Appl. Catal. B: Environ. 134 (2013) 198.
- [19] X.F. Chen, J.S. Zhang, X.Z. Fu, M. Antonietti, X.C. Wang, J. Am. Chem. Soc. 131 (2009) 11658.
- [20] G. Liu, P. Niu, C.H. Sun, S.C. Smith, Z.G. Chen, G.Q. Lu, J. Am. Chem. Soc. 132 (2010) 11642.
- [21] Y.J. Zhang, T. Mori, J.H. Ye, M. Antonietti, J. Am. Chem. Soc. 132 (2010) 6294.
- [22] M. Zhang, X.J. Bai, D. Liu, J. Wang, Y.F. Zhu, Appl. Catal. B: Environ. 164 (2015) 77.
- [23] A.M. Cant, F.Z. Huang, X.L. Zhang, Y. Chen, Y.B. Cheng, R. Amal, Nanoscale 6 (2014) 3875.
- [24] J. Ding, Q.Q. Liu, Z.Y. Zhang, X. Liu, B.N. Zong, W.L. Dai, Appl. Catal. B: Environ. 165 (2015) 511.
- [25] Z.Y. Zhang, J.D. Huang, Q. Yuan, B. Dong, Nanoscale 6 (2014) 9250.
- [26] F. Chang, Y.C. Xie, C.L. Li, J. Chen, J.R. Luo, X.F. Hu, Appl. Surf. Sci. 280 (2013) 967.
- [27] E.M. Ferrero, Y. Sakatani, C. Boissière, D. Grosso, A. Fuertes, J. Fraxedas, Adv. Funct. Mater. 17 (2007) 3348.
- [28] J. Xu, H.T. Wu, X. Wang, B. Xue, Y.X. Li, Y. Cao, Phys. Chem. Chem. Phys. 15 (2013) 4510.
- [29] X.J. Bai, L. Wang, R.L. Zong, Y.F. Zhu, J. Phys. Chem. C 117 (2013) 9952.
- [30] D.D. Zheng, C.J. Huang, X.C. Wang, Nanoscale 7 (2015) 465.
- [31] K.N. Ali, M. Divar, F. Panahi, RSC Adv. 5 (2015) 2223.
- [32] V.N. Khabashesku, J.L. Zimmerman, J.L. Margrave, Chem. Mater. 12 (2000) 3264.
- [33] X.F. Li, J. Zhang, L.H. Shen, Y.M. Ma, W.W. Lei, Q.L. Cui, Appl. Phys. A 94 (2009) 387.
- [34] M.J. Bojdy, J.O. Müller, M. Antonietti, A. Thomas, Chem. Eur. J. 14 (2008) 8177.
- [35] P.V. Zinin, L.C. Ming, S.K. Sharma, V.N. Khabashesku, X.R. Liu, S.M. Hong, Chem. Phys. Lett. 472 (2009) 69.
- [36] J.H. Li, B. Shen, Z.H. Hong, B.Z. Lin, B.F. Gao, Y.L. Chen, Chem. Commun. 48 (2012) 12017.
- [37] F. Dong, L.W. Wu, Y.J. Sun, M. Fu, Z.B. Wu, S.C. Lee, J. Mater. Chem. 21 (2011) 15171.
- [38] Y.L. Gu, L.Y. Chen, L. Shi, J.H. Ma, Z.H. Yang, Y.T. Qian, Carbon 13 (2003) 2674.
- [39] S.N. Talapaneni, S. Anandan, G.P. Mane, C. Anand, D.S. Dhawale, S. Varghese, J. Mater. Chem. 22 (2012) 9831.
- [40] J. Wei, P. Hing, Z.Q. Mo, Surf. Interface Anal. 28 (1999) 208.
- [41] A.B. Chen, Y.F. Yu, H.J. Lv, Y.Y. Wang, S.F. Shen, Y.Q. Hu, J. Mater. Chem. A 1 (2013) 1045.
- [42] S.S. Park, S.W. Chu, C. Xue, D. Zhao, C.S. Ha, J. Mater. Chem. 21 (2011) 10801.
- [43] E.R. Pinero, D.C. Amorós, A.L. Solano, J. Find, U. Wild, I.R. Schlog, Carbon 40 (2002) 597.
- [44] C.R. Clayton, Y.C. Lu, J. Electrochem. Soc. 133 (1986) 2465.
- [45] T.L. Barr, J. Vac. Sci. Technol. A 9 (1999) 1793.
- [46] K.X. Li, L.S. Yan, Z.X. Zeng, S.L. Luo, X.B. Luo, X.M. Liu, Appl. Catal. B: Environ. 156–157 (2014) 141.
- [47] E. Grabowska, J.W. Sobczak, M. Gazda, A. Zaleska, Appl. Catal. B: Environ. 117–118 (2012) 351.
- [48] X. Zhang, L.Z. Zhang, T.F. Xie, D.J. Wang, J. Phys. Chem. C 113 (2009) 7371.
- [49] S. Tonda, S. Kumar, S. Kandula, V. Shanker, J. Mater. Chem. A 2 (2014) 6772.
- [50] X.L. Yang, W.L. Dai, R.H. Gao, H.X. Li, Y. Cao, K.N. Fan, J. Mol. Catal. A: Chem. 241 (2005) 205.
- [51] Y.J. Zhang, G.H. Zhao, Y.N. Zhang, X.F. Huang, Green Chem. 16 (2014) 3860.
- [52] C.P. Liu, H.L. Lin, S.M. Gao, P.Y. Yin, L. Guo, B.B. Huang, Bull. Kor. Chem. Soc. 35 (2014) 441.
- [53] L. Wang, J.H. Zhan, W.L. Fan, G.W. Cui, H.G. Sun, L.H. Zhuo, Chem. Commun. 46 (2010) 8833.